Femtosecond strong-field quantum control with sinusoidally phase-modulated pulses

M. Wollenhaupt, A. Präkelt, C. Sarpe-Tudoran, D. Liese, T. Bayer, and T. Baumert
Institute of Physics and Center for Interdisciplinary Nanostructure Science and Technology (CINSaT), University of Kassel, Heinrich-Plett-Str. 40, D-34132 Kassel, Germany
(Received 24 April 2006; published 19 June 2006)

The quantum control of the ionization of potassium atoms using shaped intense femtosecond laser pulses is investigated. We use sinusoidal phase modulation as a prototype for complex shaped pulses to investigate the physical mechanism of the strong-field quantum control by shaped femtosecond light fields. The influence of all parameters characterizing the sinusoidal phase modulation on strong-field-induced dynamics is studied systematically in experiment and theory. Our results are interpreted in terms of the selective population of dressed states (SPODS) which gives a natural physical picture of the dynamics in intense laser fields. We show that modulated femtosecond pulses in combination with photoelectron spectroscopy are a versatile tool to prepare and to probe SPODS. The decomposition of the excitation and ionization process induced by shaped pulses into elementary physically transparent steps is discussed.

DOI: 10.1103/PhysRevA.73.063409 PACS number(s): 32.80.Qk

INTRODUCTION

One of the intriguing aspects of quantum control is the ability to manipulate quantum systems with suitably tailored laser light fields almost at will. For instance, shaped pulses are employed to guide a quantum system from an initial state to a preselected final state with high efficiency. In recent years, numerous quantum control schemes have been proposed and successfully demonstrated which are reported in recent monographs and reviews [1–5]. Besides quantum control schemes based on the detailed knowledge of the potentials and the use of simple pulse sequences, adaptive pulse manipulation using complex pulse shapes has opened new perspectives for quantum control [6]. The combination of pulse-shaping techniques [7] with closed loop adaptive feedback learning algorithms allows us to optimize virtually any conceivable observable [8–18] with applications ranging from laser science, quantum optics, atomic and molecular physics, solid state physics, photochemistry to biophysics, or quantum computing. However, it is not always possible to deduce the underlying physical mechanism from the electrical fields obtained by this procedure. Therefore, the need to bridge the gap between the efficient "black box" closed loop optimal control methods and detailed understanding of the physical processes—especially in strong laser fields—is quite evident.

Generally, weak-field control schemes are not applicable for intense laser fields where perturbation theory is no longer valid as exemplified on a generic example of ultrafast strong-field coherent control [19]. However, some of the principles of weak-field excitation are applicable to nonperturbative control employing so-called *real* pulses [20]. In this context *real* or *complex* pulses are defined by the properties of their temporal phase which determines whether the pulse envelope is real or complex valued. For example, in this context, linearly chirped pulses are *complex* whereas third order dispersion (TOD) produces *real* pulses. The implications of *real* or *complex* pulses with respect to the manipulation of the symmetry of photoelectron spectra was recently discussed in [21] in terms of selective population of dressed states (SPODS). It was found that the control of a dressed state population requires the use of *complex* fields, i.e., fields which allow phase changes in time domains be they either continuous such as linear chirps [21] or noncontinuous such as the phase jumps in a pulse sequence [3].

In this contribution we investigate control of multiphoton ionization of potassium atoms excited by well-characterized intense phase-modulated laser pulses with regard to a detailed analysis of the physical mechanism of strong-field optimal control. Atoms serve as a well-defined model system for multiphoton excitation and can be considered as a first approximation to more complex situations. Results obtained for such model systems can be generalized to multiphoton resonant excitation with no intermediate resonances [22,23]. For excitation, we use femtosecond laser pulses sinusoidally phase modulated in the frequency domain which allows us to switch from *real* to *complex* pulses. By the choice of the modulation parameters the temporal pulse structure varies from simple pulse sequences with well-defined relative phases to prototypes of complex shaped pulses reminiscent of laser fields obtained by adaptive control. The frequent use of sinusoidal spectral phase modulation in recent quantum control experiments [14,20,24–29] underscores the importance of analyzing the physical mechanisms of quantum control exerted by sinusoidal spectral phase shaping in some detail. To this end, we systematically study the influence of all relevant control parameters of the sine function in a strong-field experiment. In addition to previous experimental studies using sinusoidal phase modulation [29], the underlying physical mechanisms are discussed in some detail using different physical pictures such as the bare states, the dressed states, and the Bloch vector in order to emphasize the diverse aspects of the dynamics. We show that SPODS is operative for off-resonant excitation, which indicates that this control mechanism is robust with respect to the experimental parameters and, therefore, likely to be operative in many other real applications. For instance, applications of SPODS to the control of chemical reactions were discussed on a generic model molecule [30] and on potassium dimers [31].

The paper is organized as follows. First, the idea of the experiment is discussed in the theoretical Sec. I. Here we discuss the excitation and ionization scheme along with the simulations of the photoelectron spectra. In Sec. II the experimental strategy and the setup are described. The experi-

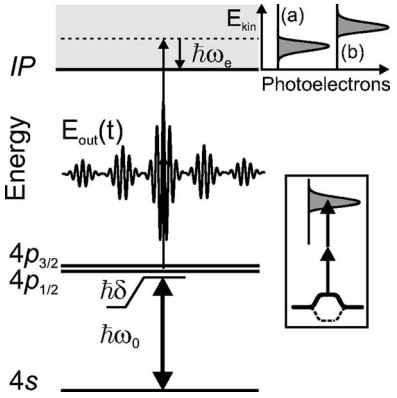

FIG. 1. Energy level diagram for excitation of K atoms. Shaped laser pulses with an electric field $E_{out}(t)$ and a carrier frequency ω_0 (corresponding to 785 nm) detuned by δ from the resonance frequencies (767 and 770 nm) create a coherent superposition of the lower $4s$ and the upper $4p$ states of K atoms (bold arrows). Spectra of the photoelectrons with a kinetic energy $E_{kin}=\hbar\omega_e$ from simultaneous two-photon ionization (light arrows) of the $4p$ state are measured. The shape of the photoelectron spectra, e.g., (a) slow or (b) fast photoelectrons, is controlled by a variation of the pulse structure. The inset illustrates the creation of fast photoelectrons from the upper dressed state corresponding to (b).

mental results from quantum control exerted by sinusoidal phase modulation in frequency domain are presented in Sec. III and discussed for the idealized case of resonant excitation in Sec. IV. The relation of the population of dressed states, the photoelectron spectra, and the dynamics of the Bloch vector are summarized in the Appendix.

I. PRINCIPLE OF THE EXPERIMENT

In this section we discuss the excitation and ionization scheme of potassium atoms used in our experiment (Sec. I A) and report how simulations of the dynamics and the photoelectrons are performed. In view of a detailed physical picture of the control mechanism the properties of the temporal electrical field obtained by sinusoidal phase modulation in frequency domain are described in some detail in Sec. I B.

A. Excitation and ionization scheme

Figure 1 shows the excitation scheme used in this experiment. Unlike conventional pump-probe scenarios in which the first pump pulse initiates the dynamics which is probed by a second pulse, in our experiment, the same pulse is used to drive the dynamics in the neutral atom and to simultaneously cause ionization. Our experiments are described theoretically by solving the time-dependent Schrödinger equation for the light induced neutral atomic dynamics in order to consider strong-field effects. Photoionization is treated using perturbation theory since the neutral-to-ionic transitions are much weaker than, for instance, the K ($4p \leftarrow 4s$) transitions. The amplitudes $c(\omega_e)$ for photoelectrons with kinetic energy $\hbar\omega_e$ for the ionization from the $4p$ excited state with an energy of $\hbar\omega_{4p}$ read [32–34]

$$c(\omega_e) \propto \int_{-\infty}^{\infty} c_b(t)[E^-(t)]^2 e^{i(\omega_e+\omega_{IP}-\omega_{4p})t} dt, \tag{1}$$

where $\hbar\omega_{IP}$ describes the ionization energy, $c_b(t)$ the time-dependent excited state amplitude, and $E^-(t)$ the (negative frequency) analytic electrical field [35] used in quantum mechanics to describe the light absorption in the rotating wave approximation. From Eq. (1) it is seen that the amplitudes $c(\omega_e)$ are the Fourier transform of the excited state amplitude $c_b(t)$ windowed by the square of the electrical field $[E^-(t)]^2$. As a consequence, the quantum mechanical phase information of the excited state amplitudes is preserved to some extent in the photoelectron spectrum. Similar to the modification of the laser pulse shape in time domain by phase modulation in frequency domain the shape of the photoelectron spectrum, i.e., $|c(\omega_e)|^2$ is modified by the temporal phase of the amplitude $c_b(t)$. The simultaneous excitation and ionization technique therefore permits us to use photoelectron spectra as a fingerprint of the quantum mechanical phase imparted by the interaction with the shaped laser pulse and therefore delivers detailed information on the dynamics which is not available in conventional pump-probe experiments. In particular, as will be shown below, the photoelectron spectra map dressed state population. During the time evolution, the dressed states are characterized by a time-dependent energy splitting $\hbar\Omega$ giving rise to the observed Autler-Townes (AT) splitting [36] in the photoelectron spectra. Employing two-photon ionization as the nonlinear probe step precludes averaging over the intensity distribution within the laser focus since the ionization probability is highest in the spatial region of highest laser intensity. This technique permits us to overcome the common problem of washing out intensity dependent strong-field effects.

B. Sinusoidal phase modulation

Since the physical mechanism of quantum control using sinusoidal phase modulation in the frequency domain are discussed in time domain as well, the important properties of the modulated pulses are summarized in this section. We start with the unmodulated (positive frequency) analytic electrical $E^+(t)=[E^-(t)]^*$ field used in ultrafast optics [35]

$$E_{in}^+(t) = \mathcal{E}_{in}^+(t) e^{i\omega_0 t}, \tag{2}$$

where ω_0 is the carrier frequency and $\mathcal{E}_{in}^+(t)$ denotes the, in general, complex electric field envelope, i.e., $\mathcal{E}_{in}^+(t)=|\mathcal{E}_{in}^+(t)|e^{i\chi_{in}(t)}$ which includes the time-dependent optical phase function $\chi_{in}(t)$. In the frequency domain, the phase function

$$\varphi(\omega) = A \sin[(\omega-\omega_{ref})T+\phi] \tag{3}$$

modulates the spectrum $\tilde{E}_{in}^+(\omega)$ such that

$$\tilde{E}_{out}^+(\omega) = \tilde{E}_{in}^+(\omega) e^{iA \sin[(\omega-\omega_{ref})T+\phi]}, \tag{4}$$

where A describes the amplitude of the phase modulation function, T the frequency of the sinusoidal oscillation, and ϕ an absolute phase offset. In view of the experimental imple-

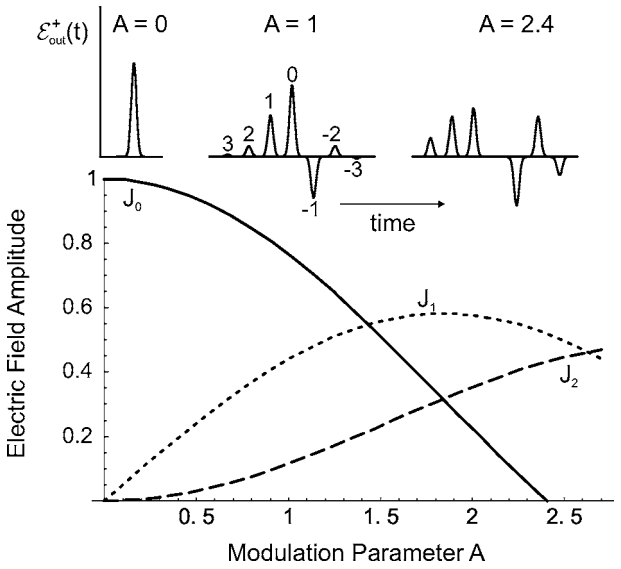

FIG. 2. Envelopes $\mathcal{E}^+_{out}(t)$ of spectrally modulated pulses. The amplitudes of the subpulses for sinusoidal phase modulation in frequency domain are described by the Bessel functions $J_n(A)$, cf. lower panel. Assuming a real unmodulated field envelope $\mathcal{E}^+_{in}(t)$ and $\Delta\omega T+\phi=0$, the modulated electrical field envelope $\mathcal{E}^+_{out}(t)$ is plotted for the values 0, 1, and 2.4 of the modulation parameter A. For $A=1$ the indices $n=-3-3$ are plotted on top of the subpulses envelopes $\mathcal{E}^+_{in}(t+nT)$. The change of sign of the envelope of the odd postpulses is due to the property $J_{-n}(z)=(-1)^n J_n(z)$ of the Bessel function. At the zero of the Bessel function J_0 at $A\approx 2.4$ the central subpulse $(n=0)$ vanishes. The time separation between the subpulses T was chosen to exceed the pulse width. In this case, the parameters $\Delta\omega$ and ϕ which control the relative phase of the subpulses do not influence the field envelope $|\mathcal{E}^+_{out}(t)|$.

mentation of spectral phase modulation by a phase mask, ω_{ref} is introduced to describe the origin of the sine function with respect to the laser spectrum. Using the Jacobi-Anger identity [37]

$$e^{iA\,\sin(\zeta)}=\sum_{n=-\infty}^{\infty} J_n(A)e^{in\zeta}, \tag{5}$$

where J_n describes the Bessel function of the first kind and order n, the phase modulated electric field in the time domain reads

$$E^+_{out}(t)=e^{i\omega_0 t}\sum_{n=-\infty}^{\infty} J_n(A)\mathcal{E}^+_{in}(t+nT)e^{in(\Delta\omega T+\phi)}, \tag{6}$$

where $\Delta\omega=\omega_0-\omega_{ref}$ describes the difference between the laser carrier frequency ω_0 and the reference frequency of the phase modulation function ω_{ref}. From Eq. (6) it is seen that sinusoidal phase modulations in frequency domain produce a sequence of subpulses with a temporal separation determined by the parameter T and well-defined relative optical phases. Provided the individual subpulses are temporally separated, i.e., T is chosen to exceed the pulse width, the envelope of each subpulse is a (scaled) replica of the unmodulated pulse envelope $\mathcal{E}^+_{in}(t)$. Figure 2 shows the amplitudes $J_n(A)$ of the subpulses as a function of the modulation parameter A and

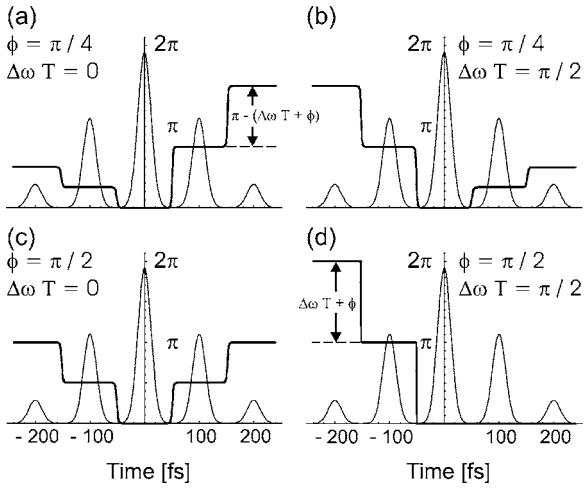

FIG. 3. Absolute temporal optical phase $\chi_{out}(t)$ (bold) and pulse envelope $|\mathcal{E}^+_{out}(t)|$ for a sinusoidally modulated 20 fs (FWHM) Gaussian pulse. The parameters for the phase modulation function $\varphi(\omega)=A\,\sin[(\omega-\omega_{ref})T+\phi]$ are $A=1$ and $T=100$ fs. The phase difference between adjacent prepulses is $\Delta\omega T+\phi$ [cf. (d)] and for adjacent postpulses $\pi-(\Delta\omega T+\phi)$ [cf. (c)] due to the extra π phase jump from the alternating sign of the Bessel functions. (a) "Pure sine" modulation with the origin of the sine function at the central frequency, i.e., $\Delta\omega=0$ and $\phi=0$. The temporal phase jumps of $\pm\pi$ are exclusively due to the alternating sign of the Bessel functions as illustrated in Fig. 2. (b) Pure cosine modulation, i.e., $\phi=\pi/2$ with relative temporal phase jumps of $\pm\pi/2$. In the right column the modulation function is displaced from the central frequency by $\Delta\omega T=\pi/2$ and absolute phases are $\phi=\pi/4$ (b) and $\phi=\pi/2$ (d).

some examples of modulated electrical field envelopes $\mathcal{E}^+_{out}(t)$

$$\mathcal{E}^+_{out}(t)=\sum_{n=-\infty}^{\infty} J_n(A)\mathcal{E}^+_{in}(t+nT)e^{in(\Delta\omega T+\phi)}. \tag{7}$$

Since the temporal optical phase of the light field is relevant to quantum control, the phase $\chi_{out}(t)$ of the modulated field envelope $\mathcal{E}^+_{out}(t)=|\mathcal{E}^+_{out}(t)|e^{i\chi_{out}(t)}$ is depicted in Fig. 3 for different values of ϕ and $\Delta\omega T$, in addition. Again, we consider fully separated subpulses such that the pulse envelope $|\mathcal{E}^+_{out}(t)|$

$$|\mathcal{E}^+_{out}(t)|=\sum_{n=-\infty}^{\infty} J_{|n|}(A)|\mathcal{E}^+_{in}(t+nT)| \tag{8}$$

is not influenced by ϕ and $\Delta\omega T$. According to Eq. (7) the absolute optical phase of the nth prepulse $(n>0)$ envelope reads $\chi_n=n(\Delta\omega T+\phi)$. Therefore the relative phase between the subpulses is determined by the phase $\Delta\chi=\Delta\omega T+\phi$. In particular, the phase difference to the adjacent prepulse is $\Delta\omega T+\phi$ as seen in Fig. 3(d). For postpulses $(n<0)$, the extra phase jump of π due to the alternating sign of the Bessel functions $J_{-n}(z)=(-1)^n J_n(z)$ needs to be taken into account in addition. This results in a phase difference of adjacent postpulses of $\pi-(\Delta\omega T+\phi)$ [cf. Fig. 3(c)]. Accordingly, phase jumps of π, i.e., the change of sign of the envelope $\mathcal{E}^+_{out}(t)$, are introduced either by the phases ϕ and $\Delta\omega=0$ or the am-

plitudes of the Bessel functions. From Eq. (7) it is also seen that if the origin of the sine function is located at the central frequency, i.e., $\Delta\omega=0$, the parameter T has no influence on the phase of modulated field envelope $\mathcal{E}^+_{out}(t)$. If, in addition, the absolute phase ϕ is set to zero—which could be referred to as "pure sine modulation"—the phase mask is antisymmetrical with respect to the carrier frequency. Provided $\mathcal{E}^+_{in}(t)$ is real, the modulated field $\mathcal{E}^+_{out}(t)$ is also real and the phase between adjacent post subpulses jumps by π due to change of sign introduced by the Bessel functions as shown in Fig. 3(a). For $\Delta\omega=0$, a "pure cosine modulation" is implemented by $\phi=\pi/2$. In this case the modulation function is symmetrical with respect to the carrier frequency and therefore the modulated field $\mathcal{E}^+_{out}(t)$ is *complex* even for a real unmodulated field $\mathcal{E}^+_{in}(t)$. As an example, it follows from the Taylor expansion of the cosine function $\cos(\varphi)\approx 1-\varphi^2/2$ that in the limit of low values of T but high values of A this type of phase modulation mimics a linear chirp epitomizing pulses with complex valued envelopes. Figure 3(b) shows that the phase of the nth subpulse is $n\pi/2$ which introduces phase factors of $e^{in\pi/2}=\pm\sqrt{\pm 1}$, i.e., ± 1 and $\pm i$. Hence, the square of the modulated field $[\mathcal{E}^+_{out}(t)]^2$ is real. This is only true if the subpulses are fully separated in time. Otherwise the "pure cosine" modulation leads to complex second harmonic fields. Real cosine modulated second harmonic fields were employed in [20] to control a two-photon transition in strong laser fields with a *real* second harmonic—but *complex* fundamental—field. As soon as the sine function is shifted from the central frequency ($\Delta\omega\neq 0$), the parameter T controls both the temporal separation and the phase via the phase factor $e^{i\Delta\omega T}$ in Eq. (7).

C. Numerical simulations

In order to compare our experimental results to simulations, we model the excitation and ionization dynamics using a three-level system weakly coupled to a flat continuum. In Sec. III we consider the $4p_{1/2}\leftarrow 4s_{1/2}$ and $4p_{3/2}\leftarrow 4s_{1/2}$ transitions excited by linear polarized laser light. The initial unmodulated electric field $\mathcal{E}^+_{in}(t)$ has a Gaussian spectrum and its phase is modulated in frequency domain to calculate $\mathcal{E}^+_{out}(t)$. The strong-field dynamics in the off-resonant three-level system is calculated by the numerical solution of the time-dependent Schrödinger equation (TDSE) using a short time propagator method [28].

In order to extract the essential physical mechanisms, we consider the resonant excitation of a two-level system in the discussion (Sec. IV). In this case analytic solutions of the TDSE are available [38] provided the subpulses are fully separated. In both cases Eq. (1) is employed to calculate the photoelectron spectra using efficient Fourier techniques [33]. In the theoretical considerations, ionization can be turned on and off in certain time intervals to yield a partial photoelectron spectrum due to ionization of a single subpulse. This serves as a tool to analyze the structure of the observed photoelectron spectra.

II. EXPERIMENT

In Sec. II A the experimental strategy to provide a comprehensive account to the control attainable using sinusoidal phase modulation is presented. Details of the setup are presented in Sec. II B.

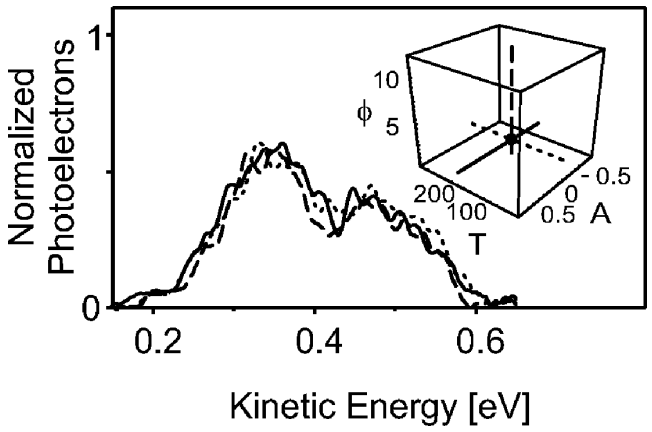

FIG. 4. Measured photoelectron spectra for sinusoidal phase modulation at the point of the intersection of the three scans of time T, amplitude A, and phase ϕ at $A=-0.2$, $T=170$ fs, and $\phi=1.7$ rad. Each scan is indicated in the three-dimensional parameter space as shown in the inset, i.e., the variation of T for fixed A and ϕ (dotted), the variation of A for fixed T and ϕ (bold), and the variation of ϕ for fixed A and T (dashed). The agreement of all spectra demonstrates the reproducibility of the experimental results.

A. Experimental strategy

A complete investigation of the effect of sinusoidal phase modulation of the form $\exp\{iA\sin[(\omega-\omega_{ref})T+\phi]\}$ requires the measurement of photoelectron spectra for each point in the three-dimensional parameter space spanned by A, T, and ϕ as shown in the inset to Fig. 4. In order to reduce the amount of data we performed a series of measurements for the independent control parameters time T, amplitude A, and phase ϕ along each dimension of the parameter space while the intensity I_0 and the reference frequency $\omega_{ref}=2.4$ rad/fs were unchanged. The parameters for each scan were so chosen that the three scans intersect at $A=-0.2$, $T=170$ fs, and $\phi=1.7$ rad. This procedure allows us to check the reproducibility of our experimental results. The agreement of all spectra shown in Fig. 4 demonstrates the fidelity of the phase modulator as well as the stability of the laser parameters such as intensity, pointing stability, and chirps during the course of the experiments. The photoelectron spectra obtained in each scan are discussed in Secs. III A–III C.

B. Experimental setup

The experimental setup is shown in Fig. 5. Femtosecond laser pulses of 30 fs full width at half maximum (FWHM) duration at a mean wavelength of $\lambda_0=785$ nm with a repetition rate of 1 kHz were generated by a Ti:sapphire multipass amplifier. We employed our homebuilt pulse shaper [39] to modulate the femtosecond laser pulses. A 128 pixels liquid crystal spatial light modulator served as the computer-controlled spectral mask in the pulse-shaping setup. The modulated pulses were focused into a vacuum chamber by a 300 mm lens. Here, the femtosecond pulses interacted with a

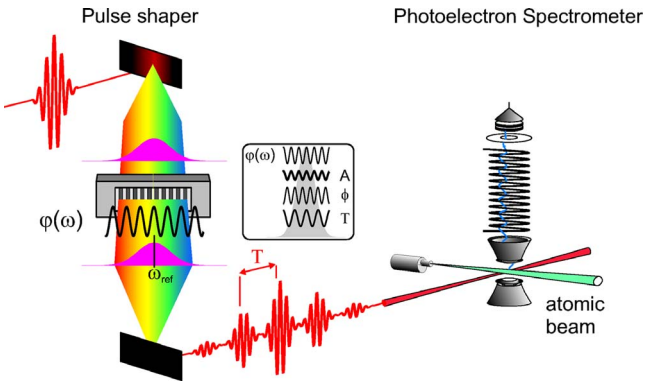

FIG. 5. (Color online) Experimental setup: femtosecond laser pulses from a Ti:sapphire amplifier were spectrally phase-modulated using sinusoidal phase modulation functions of the form $\varphi(\omega)=A\sin[(\omega-\omega_{ref})\cdot T+\phi]$ centered at the reference frequency ω_{ref} in our pulse shaper. The inset shows phase functions $\varphi(\omega)$ for different A, ϕ, and T on top of the laser spectrum (gray shaded). The modulated laser beam was focussed into a vacuum chamber to interact with a potassium atomic beam. Photoelectron kinetic energy spectra were recorded employing a magnetic bottle spectrometer (right).

potassium atomic beam generating photoelectrons. Kinetic energy time-of-flight spectra of the photoelectrons were recorded by a magnetic bottle spectrometer. The potassium atomic beam was generated using an oven at a temperature of 360 °C with an exiting nozzle of 200 μm diameter. The vacuum chamber pressure was 1.3×10^{-6} mbar. The femtosecond beam waist radius of 30 μm in the interaction area was measured by a cutting knife method. In the experiment, we set the pulse energy to 0.35 μJ, corresponding to an intensity of about 4×10^{11} W/cm^2. In order to characterize the shaped laser pulses we employed spectral [41], temporal [35], and spectrogram-based [42] pulse characterization techniques because a single method may not be sufficient to provide reliable results for the whole parameter range of the sinusoidal spectral phase modulation. First, we ensure the functionality of our pulse by measuring short pulses with a duration adapted to the spectrogram window. To this end, the phase function is set to $\varphi(\omega)=1.5\sin[60\text{ fs}(\omega-2.4\text{ rad/fs})+\pi$. The results from the retrieval using spectrogram-based techniques are depicted in Fig. 6(a). In this figure the temporal electric field and phase of a spectrally sinusoidally shaped pulse are shown along with the calculated results using the measured spectrum and experimental phase modulation parameters. It is seen that the sinusoidal spectral modulation generates a pulse sequence in time domain with the inter-subpulse-distance of $T=60$ fs as expected from the theoretical discussion in Sec. I B. The temporal phase shows jumps between the subpulses in agreement with the calculations. A pulse with a duration exceeding the time window of the spectrogram generated by $\varphi(\omega)=0.8\sin[200\text{ fs}(\omega-2.424\text{ rad/fs})]$ is characterized in the spectral domain. Spectral interference of the modulated and unmodulated pulse enable us to investigate the accuracy of the pulse shaper since spectral characterization techniques measuring the *additional* phase introduced by the shaper with high accuracy. Figure 6(b) shows the power spectral density, the

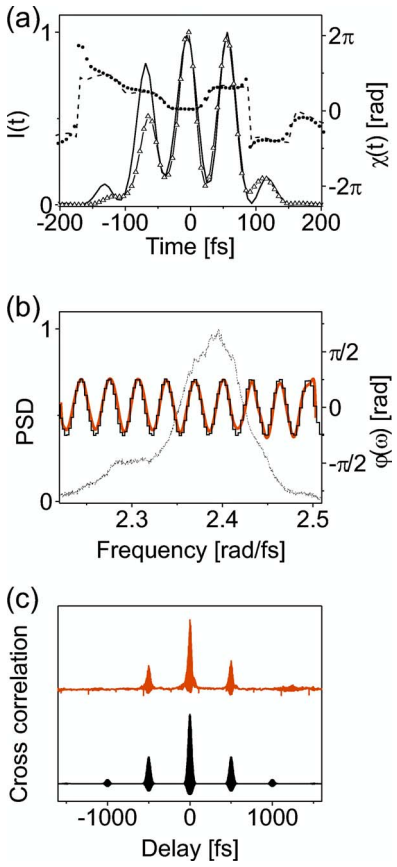

FIG. 6. (Color online) Characterization laser pulses subjected to sinusoidal spectral phase modulation using (a) spectrogram-based, (b) spectral, and (c) temporal techniques. (a) Retrieved temporal signal from the spectrogram: normalized intensity (solid line measured, white triangles calculated using measured spectrum and experimental phase modulation parameters) and phase (dashed line measured, black dots calculated as above) for $\varphi(\omega)=1.5\sin[60\text{ fs}(\omega-2.4\text{ rad/fs})+\pi]$, (b) spectral interference: spectrum (thin line), measured (orange solid line) and applied (solid line) spectral phase $\varphi(\omega)=0.8\sin[200\text{ fs}(\omega-2.424\text{ rad/fs})]$, (c) second harmonic cross correlation: measured (orange, upper) and simulated (black, lower) for $\varphi(\omega)=\sin[500\text{ fs}(\omega-2.4\text{ rad/fs})]$.

sinusoidal spectral phase set by the pulse shaper, and the spectral phase as retrieved by spectral interference. Good agreement proves high accuracy of the spectral phase introduced by the pulse shaper. However, spectral methods do not give a direct picture of the temporal shape of the pulse particularly if the pulse spectra are distorted. In order to directly map out the temporal structure of a pulse that spans 2 ps created by the modulation function $\varphi(\omega)=\sin[500\text{ fs}(\omega-2.4\text{ rad/fs})]$ we measure the second harmonic cross correlation with the unmodulated 30 fs pulse. Measured and simulated cross correlations of a sinusoidally shaped pulse depicted in Fig. 6(c) show good agreement.

III. RESULTS

The experimental photoelectron spectra obtained by variation of the control parameters of the phase modulation func-

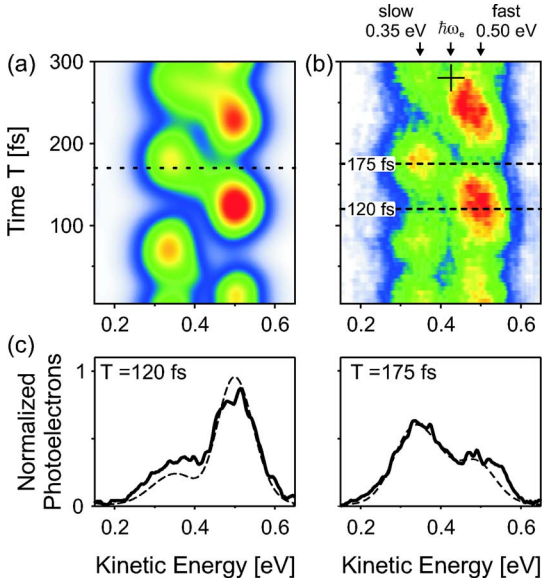

FIG. 7. (Color online) (a) Simulated and (b) measured photoelectron spectra upon variation of the parameter T within 5–300 fs for fixed values of $A=-0.2$ and $\phi=1.7$ rad. The dashed line in (a) indicates the reference point at $T=170$ fs. In the lower panel (c) sections through the photoelectron distributions of (a) and (c) at $T=120$ fs (left) and $T=175$ fs (right) as indicated by the lines in (b) show the experimental results (bold lines) and the simulated photoelectron spectra (dashed lines). In (b) the energy of the slow photoelectrons at 0.35 eV, the fast photoelectrons at 0.50 eV, and the excess energy for weak-field ionization $\hbar\omega_e$ are also indicated. The cross hairs in (b) indicates an additional structure in the photoelectron spectra due to the fine structure splitting.

tion, i.e., the temporal separation of the individual subpulses T, the absolute phase ϕ, and the modulation amplitude A are discussed in this section. The experimental results are compared to simulations (cf. Sec. I C) in which the phase modulation parameters, i.e., T, ϕ, A, and $\Delta\omega$ were directly taken from the experimental settings. The energy resolution of our photoelectron spectrometer was taken into account by convolution of the calculated spectra with a 60 meV FWHM Gaussian spectrum. In all the simulations the laser parameters such as the spectrum, the intensity, and the chirp parameters were identical. We derive the temporal pulse shape from the measured laser spectrum and allow for a small residual uncompensated chirp (<100 fs^2 corresponding to the chirp introduced by 2 mm BK7 glass) in the interaction region. The laser intensity is derived from the measured AT splitting. Therefore, the residual uncompensated chirp is the only free parameter to model the three independent two-dimensional sets of measurements shown in Figs. 7–9. In addition to the reproduction of the experimental data, the simulations were used to assess the sensitivity of the results with respect to the phase mask parameters and the laser parameters on the one hand, and the physical model, e.g., the influence of the fine structure splitting, on the other. This procedure serves to identify the physical origin of the observed features.

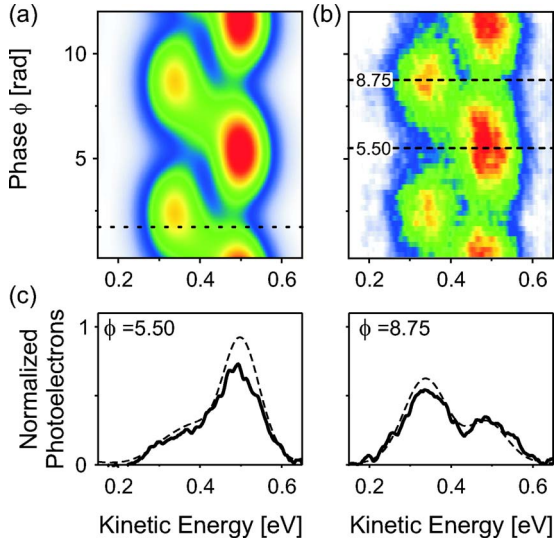

FIG. 8. (Color online) (a) Simulated and (b) measured photoelectron spectra upon variation of the parameter ϕ within 0.25–12.25 rad for fixed values of $A=-0.2$ and $T=170$ fs. The dashed line in (a) indicates the reference point at $\phi=1.7$ rad. In the lower panel (c) sections through the photoelectron distributions of (a) and (b) at $\phi=5.50$ rad (left) and $\phi=8.75$ rad (right) as indicated by the lines in (b) show the experimental results (bold lines) and the simulated photoelectron spectra (dashed lines).

A. Control exerted by the time T

First, we study the photoelectron spectra upon variation of the control parameter T. In the range of $T=0$–300 fs time of flight spectra are recorded in steps of $\Delta T=5$ fs. These spectra

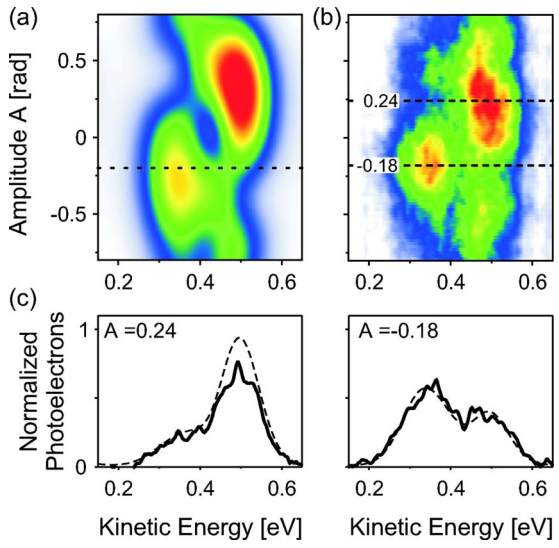

FIG. 9. (Color online) (a) Simulated and (b) measured photoelectron spectra upon variation of the parameter A within -0.8–0.8 for fixed values of $\phi=1.7$ rad and $T=170$ fs. The dashed line in (a) indicates the reference point at $A=-0.2$. In the lower panel (c) sections through the photoelectron distributions of (a) and (b) at $A=0.24$ (left) $A=-0.18$ and (right) as indicated by the lines in (b) show the experimental results (bold lines) and the simulated photoelectron spectra (dashed lines).

were combined to yield a two-dimensional photoelectron distribution shown in Fig. 7 in a false color representation. For comparison, simulated and measured photoelectron spectra are shown in Figs. 7(a) and 7(b). The energy splitting of the two photoelectron maxima in the spectrum at around 0.35 eV (slow photoelectrons) and 0.50 eV (fast photoelectrons) of about 150 meV is due to the AT effect. The fine structure splitting of the K $4p$ states of $\Delta E=7.1$ meV is not resolved in the photoelectron spectra. On the average, the fast photoelectrons are slightly more intense than the slow photoelectrons. In contrast to previous measurements using pulse sequences where the intensities of slow and fast photoelectrons oscillate with the optical period (2.6 fs) [19], by variation of T these oscillations occur with a period of about 110 fs. The intensity oscillations of the slow photoelectrons are shifted by half the period, i.e., 55 fs, with respect to the oscillation of the fast photoelectrons. Independent simulations show that the oscillation period is very sensitive to the exact position of $\Delta\omega$. The above simulation results confirm the values taken from the experimental setup. By a variation of T we exert control on the population of the dressed states. The oscillations in the photoelectron distribution show that both dressed states are selectively populated. For instance, sections through the photoelectron distribution along the energy axis at $T=120$ fs and $T=175$ fs yield the photoelectron spectra shown in Fig. 7(c) which demonstrate the population of the upper and lower dressed states, respectively. Calculated and measured photoelectron spectra are in good agreement. In addition to these coarse features the detailed structure of the photoelectron spectrum is quite complicated. Most notably, the maxima of either slow or fast photoelectrons are neither exactly equidistant nor do they have equal intensity. Moreover, an additional structure at around $T=280$ fs and 0.42 eV is observed [see cross hairs in Fig. 7(b)]. The comparison with the simulation reveals that these additional structures are real physical structures. Generally, the deviations from symmetric AT spectra with equidistant maxima are a consequence of both, the actual temporal structure of the laser pulse and the energy level structure of K atoms which is not fully described by a two-level system. For instance, off-resonant excitation leads to asymmetric AT spectra. At the laser wavelength of 785 nm, which is red detuned with respect to the $4p \leftarrow 4s$ resonances, one would expect a higher ionization probability for the low energy photoelectrons. However, the experimental spectra show slightly higher intensities for the fast photoelectrons. Taking into account a residual uncompensated chirp of only 90 fs^2 in the simulations reproduces the experimental results and favors the generation of fast photoelectrons. This is a consequence of transient dressed state population due to chirped excitation [21]. In addition, the actual temporal pulse envelope, which is not perfectly Gaussian, leads to further deviations from the idealized picture. Since the dipole moments for the excitation with linear polarized light are different for both transitions $4p_{1/2} \leftarrow 4s_{1/2}$ and $4p_{3/2} \leftarrow 4s_{1/2}$, which are excited within the laser bandwidth, a three-level system is considered in our simulations. Upon comparison with a simulation using a two-level model, we find that the additional structure at $T=280$ fs and 0.42 eV is a consequence of the fine structure splitting. This is reasonable on the grounds that the observed time of 280 fs roughly corresponds to half the fine structure splitting of $\tau=2\pi\hbar/\Delta E\approx 580$ fs.

B. Control exerted by the phase ϕ

In this section, we investigate control exerted by the absolute phase ϕ of the sinusoidal modulation function. To this end, the phase is varied in a range 0.25–12.25 rad for fixed values of $A=-0.2$ and $T=170$ fs and the residual chirp of 90 fs^2. False color representations of the simulated (a) and measured (b) photoelectron spectra are presented in Fig. 8. The intensity distribution alternates between slow and fast photoelectrons upon the variation of ϕ. Sections along the kinetic energy axis at $\phi=5.50$ rad and $\phi=8.75$ rad as shown in Fig. 8(c) demonstrate our ability to switch between selective population of the upper and the lower dressed state by a variation of ϕ. Due to the 2π periodicity of the phase mask the period of the oscillatory dressed states population upon variation of ϕ is also 2π. Our simulations reproduce the absolute values of ϕ to selectively populate either dressed state, e.g., $\phi=5.50$ rad for the maximum population of the upper dressed state [cf. Fig.8(c)]. These values are highly sensitive to the value of $\Delta\omega$ as expected since the temporal phase of the subpulses is determined by $\Delta\omega T+\phi$ [see Eq. (7)]. Similar to the time variation discussed in Sec. III A, additional simulations show that the results are strongly dependent on the residual chirp of the laser pulse.

C. Control exerted by the amplitude A

Photoelectron spectra upon variation of the modulation amplitude A in a range of -0.8 to 0.8 for fixed values of $\phi=1.7$ rad and $T=170$ fs are presented in Fig. 9. A value of $A=0$ corresponds to the unmodulated pulse. With increasing A the intensity of the prepulse and postpulses increases in the same way for positive and negative values of A. However, the phase of the subpulses is different in both cases. As a consequence positive modulation amplitudes favor the population of the upper dressed state whereas the lower dressed state is preferentially populated for negative values of A as confirmed by the sections through simulated (a) and measured (b) photoelectron distributions shown in Fig. 9(c) at $A=0.24$ (left) and $A=-0.18$ (right). Again, the simulations show that the photoelectron distribution is very sensitive to the residual chirp of the laser and the offset of the phase mask $\Delta\omega$.

IV. DISCUSSION

In this section we discuss the above observations in terms of an idealized picture characterized by the resonant excitation of a two-level atom. The parameters of the spectral phase function are chosen to depict the physical mechanisms of dressed state control with greatest clarity. This approach is physically meaningful, because the photoelectron spectra are well reproduced with our models based on the strong-field interaction with a two- or three-level atom weakly coupled to the continuum. Upon comparison of the three-level model allowing for the fine structure splitting and the two-level model, we found that the fine structure splitting does not

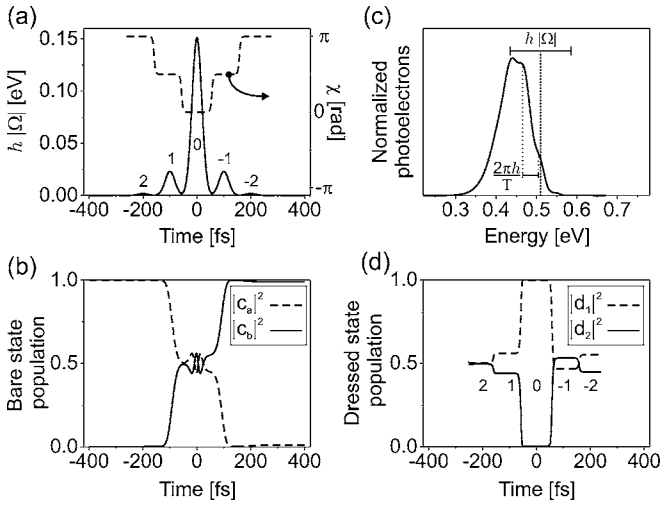

FIG. 10. Simulation for resonant strong-field excitation using a sinusoidal phase modulated 30 fs FWHM Gaussian laser pulse. The modulation parameters are $A=0.3$, $T=100$ fs, $\phi=\pi/2$ rad, and $\Delta\omega=\pi/50$ fs^{-1}. (a) Envelope of the electrical field $|\mathcal{E}^+(t)|$ in units of the AT splitting $|\hbar\Omega(t)|=|\mu\mathcal{E}^+(t)|$ (bold, left scale) and temporal phase $\chi(t)$ of the electric field (dashed, right scale). The subpulses are indicated with labels from $n=2$ to -2. (b) Time evolution of the bare state population (ground state $|c_a|^2$ dashed, and excited state $|c_b|^2$ bold). (c) Simulated photoelectron spectrum: the dashed line indicates the kinetic energy of weak-field photoionization $\hbar\omega_e$ and the bar shows the AT splitting at the most intense subpulse ($n=0$, compare value of $|\hbar\Omega(t)|$ in (a) at $t=0$). Only the low kinetic energy AT component is present in the photoelectron spectrum revealing that the lower dressed state is selectively populated during the subpulse of maximum laser intensity. The shoulders in the photoelectron spectrum with an energy separation of $2\pi\hbar/T$ arise from the interference of free electron wave packets. (d) Population of the dressed states (lower state $|d_1|^2$ dashed, and upper state $|d_2|^2$ bold).

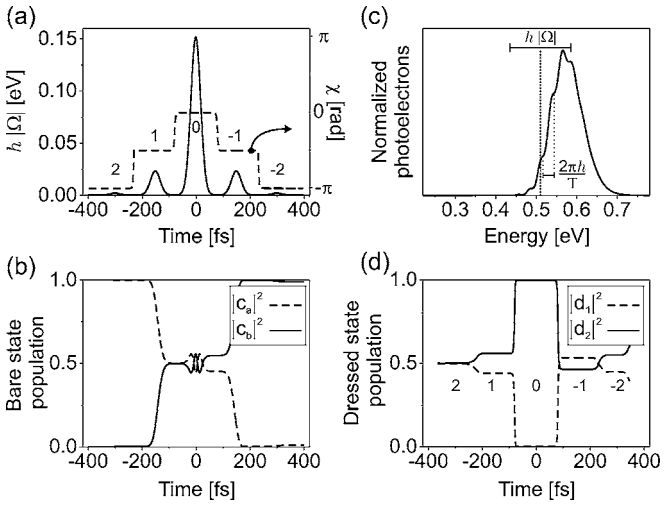

FIG. 11. Simulation for the modulation parameters $A=0.3$, $T=150$ fs, and $\phi=\pi/2$ rad. Only the high kinetic energy AT component is present in the photoelectron spectrum (c) revealing that the upper dressed state is selectively populated during the subpulses of the maximum laser intensity ($n=0$) as seen in (d). For labels see Fig. 10.

influence the essential structures of the observed photoelectron spectra. We start with the discussion of the light induced dynamics of the neutral atoms induced by sinusoidally phase-modulated 30 fs (FWHM) Gaussian laser pulses. The intensity of the laser electric field $\mathcal{E}^+(t)$ in the simulations was chosen to reproduce the experimental AT splitting of 150 meV, i.e., the Rabi frequency $\hbar\Omega=\mu\mathcal{E}^+$ for the most intense subpulse is about $\hbar\Omega=150$ meV. Figure 10 shows the results of the simulations for the modulation parameters $T=100$ fs, $\phi=\pi/2$, $A=0.3$, and $\Delta\omega=\pi/50$ fs^{-1}. This case serves as a reference to study the effect of the variation of each parameter, i.e., the time T (Fig. 11), the phase ϕ (Fig. 12), and the modulation amplitude A (Fig. 13). In all cases the neutral dynamics is discussed in terms of time-dependent Rabi frequency $\Omega(t)$, the optical phase $\chi(t)$ of the field, the bare state population $|c_a|^2$ and $|c_b|^2$ of the lower and upper states, and the population of the lower and upper dressed states $|d_1|^2$ and $|d_2|^2$. Based on the strong-field-induced neutral dynamics we interpret the resulting photoelectron spectra in terms of the dressed state population. Because the Bloch sphere picture is well suited to illustrate quantum control exerted by the temporal phase and it provides a convenient link between the bare state amplitudes and the dressed state population we visualize the above quantum control scenarios in the Bloch sphere picture in the Appendix.

Figure 10(a) shows the time-dependent Rabi frequency $\Omega(t)$, which is proportional to the driving field envelope $\mathcal{E}(t)$, and the temporal phase $\chi(t)$ of the laser electric field. As discussed in Sec. I B the modulated electrical field envelope $|\mathcal{E}^+(t)|$ consists of a sequence of five subpulses temporally separated by $T=100$ fs. The respective relative amplitudes of the subpulses are $J_0(0.3)=0.98$, $J_1(0.3)=0.15$, and $J_2(0.3)=0.01$ and the absolute temporal phase of the electrical field is determined by $\Delta\omega T+\phi$. The above values of T, ϕ, and $\Delta\omega$ implement a pure cosine modulation of the form $\varphi(\omega)=\cos[100\text{ fs}(\omega-\omega_0)]$, which leads to a similar pulse shape as

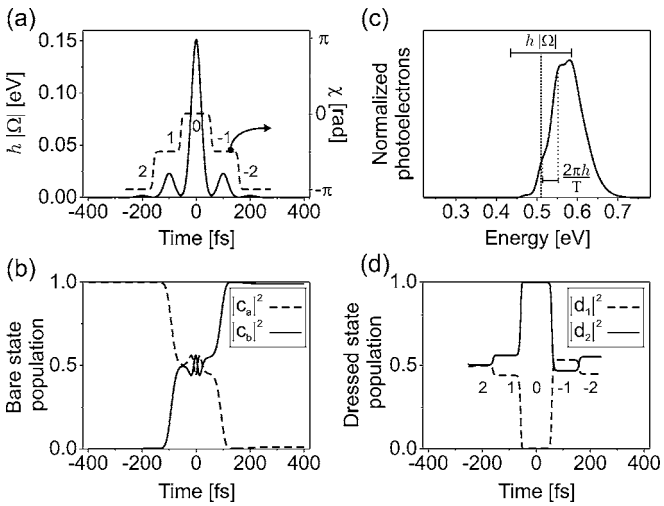

FIG. 12. Simulation for the modulation parameters $A=0.3$, $T=100$ fs, and $\phi=-\pi/2$ rad. Only the high kinetic energy AT component is present in the photoelectron spectrum (c) revealing that the upper dressed state is selectively populated during the subpulses of the maximum laser intensity ($n=0$) as seen in (d). For labels see Fig. 10.

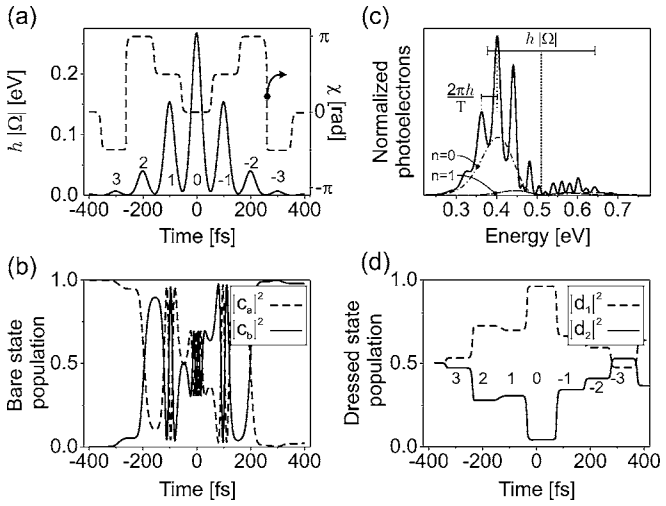

FIG. 13. Simulation for the modulation parameters $A=1$, $T=100$ fs, and $\phi=\pi/2$ rad. In order to compensate the reduction of the peak intensity due to the higher modulation amplitude (cf. Fig. 2) the laser field was increased to $2.3\times\mathcal{E}_{in}^{+}(t)$ resulting in a larger AT-splitting $\hbar|\Omega|$ of 0.27 eV (c). Predominantly, the low kinetic energy AT component is present in the photoelectron spectrum (c) revealing that the lower dressed state is more populated during the whole excitation process (d). Ionization during the prepulses and postpulses ($n\neq 0$) becomes more probable due to their increased relative intensity and therefore the interference fringes with a spacing of $2\pi\hbar/T$ are more pronounced. Partial photoelectron spectra due to the ionization during the central subpulse ($n=0$, dashed-dotted) and the ionization during the adjacent pulse ($n=1$, dashed) are shown in addition. For labels see Fig. 10.

depicted in Fig. 3(b). At each zero of the envelope, a phase jump of $\pm\pi/2$ takes place, i.e., the carrier jumps from cosine to sine. In the following, we discuss the bare state dynamics for each subpulse as shown in Fig. 10(b). The first weak subpulse ($n=2$) leaves the ground state population essentially unchanged. Therefore, the dynamics is accurately described by the perturbation theory. The second subpulse ($n=1$) with a pulse area of $\pi/2$ creates a superposition state of maximum coherence, i.e., equal population of both states $|c_a|^2=|c_b|^2=0.5$. The phase jump of $-\pi/2$ between the first and the second subpulses has no influence on the bare state dynamics induced by the second nonperturbative interaction. This is in sharp contrast to the effect of the third subpulse ($n=0$). Although this subpulse has by far the highest intensity, it leaves the population unchanged [cf. Fig. 10(b) at $t\approx 0$]. This situation is reminiscent of spin locking known from nuclear magnetic resonance [43] and phase control exerted by cw lasers [44] termed photon locking [45]. It was demonstrated in [19] that photon locking can be used for ultrafast control the quantum mechanical phase of the involved states. In the Appendix, Sec. 1 we show that this is the case for phase jumps of $\pm\pi/2$. The fourth subpulse ($n=-1$) has the same temporal phase as the second subpulse ($n=1$) [cf. Fig. 10(a)]. As a consequence, the time evolution during this $\pi/2$ pulse continues the time evolution induced by the second subpulse leading to an inversion at the end of the fourth subpulse. The final fifth subpulse is again weak enough to leave the population essentially unchanged, irrespective of its relative phase. Since the measured photoelectron spectra reveal the population of the dressed states (see the Appendix, Sec. 1), we consider the light-induced dynamics of the population in the dressed states picture as shown in Fig. 10(d). Since the excitation starts from ground state atoms, both dressed states are equally populated $|d_1|^2=|d_2|^2=0.5$ during the first subpulse. Though weak, the first subpulse creates a superposition state and, therefore, the $-\pi/2$ phase jump of the second subpulse (at -150 fs) permits us to exert control on the dressed state population, i.e., the unequal population of both dressed states. The fact that the second subpulse does not exhibit SPODS is not due to its (low) intensity, but due to the low degree of coherence produced by the first pulse. It is shown in the Appendix that besides the proper relative phase, a state of maximum coherence is required as the initial state in order to achieve SPODS during resonant excitation with a pulse of arbitrary intensity. This condition is met for the third pulse. Here the initial state is prepared in a state with $|c_a|^2=|c_b|^2=0.5$, and the phase jump of $-\pi/2$ at -50 fs leads to the selective population of the lower dressed state. Two-photon ionization is most probable during this subpulse due to its highest intensity. As a consequence, the photoelectron spectrum is largely determined by the selective population of the lower dressed state during the most intense subpulse. Indeed, the concept of the dressed state population allows us to predict the photoelectron spectrum. To this end, we consider the fact that the photoelectron spectrum maps the (transient) population of the dressed states (cf. Appendix, Sec. 1). The energy splitting $\hbar|\Omega|$ of the dressed states is extracted from the time-dependent Rabi frequencies depicted in Fig. 10(a). For instance, the photoelectron spectrum from ionizing a selectively populated lower dressed state—as shown in Fig. 10(d)—consists of a single AT component shifted towards lower energies by $\hbar|\Omega|/2=75$ meV with respect to the kinetic energy obtained by weak-field ionization $\hbar\omega_e$. This agrees well with the photoelectron spectrum obtained in the simulation using Eq. (1) as depicted in Fig. 10(c). Ionization during the pulses with $n=\pm 1$, where both dressed states are approximately equally populated, also contributes (fewer) photoelectrons. The respective maxima are displaced by $\hbar|\Omega|=\pm 12.5$ meV from $\hbar\omega_e$ [cf. $\hbar|\Omega(t)|$ at ± 100 fs in Fig. 10(a)]. Interferences of the free electron wave packets [40] created during the ionization by the subpulses before and after the central subpulse produce the shoulders in the photoelectron spectrum separated by an energy of $2\pi\hbar/T$. The weak-field interaction during the subpulses with ($n=\pm 1$) is irrelevant for the photoelectron spectrum.

It turns out that the relative phase between the prepulse which prepares the maximum coherent state ($n=1$) and the subsequent central subpulse ($n=0$) is the decisive quantity for strong-field dressed state control. In the following, this issue is illustrated on three further examples. Using the same parameters of the phase mask except for the value of T—which is now set to 150 fs—a pulse sequence as depicted in Fig. 11(a) is obtained. As discussed in Sec. I B, the subpulses are separated by 150 fs. Since $\Delta\omega$ is nonzero, the parameter T not only controls the temporal separation but the absolute temporal phase in addition. With the values of $\Delta\omega=\pi/50$ fs^{-1}, $\phi=\pi/2$, and $T=150$ fs, the modulation is of

the form $\varphi(\omega)=-\cos[150\ \text{fs}(\omega-\omega_0)]$, i.e., a negative pure cosine phase modulation, resulting in an absolute phase $n(\Delta\omega T+\phi)=-n\pi/2$, i.e., phase jumps between adjacent prepulses of $+\pi/2$. This means that by the variation of T the phase jumps change their sign compared to Fig. 10(a). The time evolution of the bare state population shown in Fig. 11(b) is very similar to that shown in Fig. 10(b), although the phases of the subpulses are quite different. This demonstrates that the bare state population is not always a suitable physical quantity to study strong-field quantum control. However, the time evolution of the dressed state population is completely inverted [cf. Fig. 10(d)]. Now, the second $\pi/2$ subpulse ($n=1$), which creates the coherent superposition state, slightly favors the upper dressed state. Due to the $\pi/2$ phase jump at -75 fs the central pulse ($n=0$) selectively populates the upper dressed state which is mapped into the photoelectron spectrum shown in Fig. 11(c). The energy separation of the shoulders in the photoelectron spectrum of $2\pi\hbar/T$ is reduced since the temporal separation T of the pulses is enlarged to 150 fs. The above analysis demonstrates how the dressed state population is controlled by the variation of the parameter T. For a constant value of ϕ, the phase jumps are controlled by $\Delta\omega T$ which implies that the oscillation period of the population of either dressed state as discussed in Sec. III A is $2\pi/\Delta\omega$. For example, the above value of $\Delta\omega=\pi/50\ \text{fs}^{-1}$ results in a period of 100 fs similar to the experimental observations. As a consequence the oscillation period is determined by the origin of the sine mask with respect to the central frequency ω_0. This explains the sensitivity of the experimental results with respect to the laser beam pointing stability because in the experiment $\Delta\omega$ is determined by the position of the spectral phase mask with respect to the laser spectrum.

An alternative way to change the relative phase between adjacent subpulses is shown in Fig. 12. Here, we use the reference parameters of Fig. 10 except for the change of sign of ϕ. By setting $\phi=-\pi/2$ we implement again a negative pure cosine phase-modulation function $\varphi(\omega)=-\cos[100\ \text{fs}(\omega-\omega_0)]$ but leave the temporal separation of the subpulses at 100 fs. Since the relative phase $\Delta\omega T+\phi$ is again $-\pi/2$ the phase jumps are identical with those shown in Fig. 11(a) but the field envelope $|\mathcal{E}^+(t)|$ is identical with Fig. 10(a). In spite of the opposite phase jumps of the field, the time evolution of the bare states shown in Fig. 12(b) is *identical* with the one presented in Fig. 10(b). The control mechanism can be inferred from the dressed state population shown in Fig. 12(d). Again by virtue of the positive phase jump at -50 fs the upper dressed state is selectively populated during the central subpulse. Because the temporal separation between the subpulses is 100 fs, like in the reference case, but the time evolution of the dressed state population is inverted, the photoelectron spectrum depicted in Fig. 12(c) is a mirror image of the spectrum shown in Fig. 10(c). These considerations show how the variation of the phase is used to exert control on the dressed state population. For a given value of$\Delta\omega$ the absolute phase ϕ directly controls the relative phase between the subpulses and therefore the oscillation period of the dressed state population is 2π in accordance with the experimental findings presented in Sec. III B.

Another way to manipulate the relative phase of the subpulses and hence the dressed state population would be the change of the sign of the modulation amplitude A as discussed in Fig. 9(c) for the experimental results. The fact that the Bessel functions are either symmetric or antisymmetric, i.e, $J_n(-A)=(-1)^nJ_n(A)$, implies that the change of sign of the amplitude only introduces additional phase jumps of π. Therefore, instead of considering the change of the sign of A, we discuss a change of the absolute value of A leaving the other phase-modulation parameters unchanged as shown in Fig. 13. When A is increased to 1, more energy is transferred to the prepulses and postpulses at the expense of the main pulse leading to a sequence of seven subpulses. To compensate for the attenuation of the central pulse as a result of the higher value of A, i.e., $J_0(1)\approx 0.76$, and in order to present a clear physical picture of the dynamics, we rise the field $\mathcal{E}_{in}^+(t)$ by a factor of $f=2.3$. This results in a larger AT splitting of about 0.27 eV as shown in Figs. 13(a) and 13(c). As a consequence, the AT splitting for the higher intensity does not directly scale with f but rather with $fJ_0(1.0)/J_0(0.3)=1.8$ due to the alternation of the modulation amplitude. This pulse sequence gives rise to a rather complicated bare state dynamic shown in Fig. 13(b). For none of the subpulses a stationary bare state population—characteristic for photon locking—is obtained. Instead, the bare state dynamic is characterized by strong Rabi oscillations typically for strong-field quantum control. In contrast to the involved features of the bare state dynamics, the dressed state time evolution is rather simple. Figure 13(d) shows that throughout (almost) the whole excitation process the population of the lower dressed state is favored. This results in a photoelectron spectrum in which the lower AT component is strongly enhanced. Details of the photoelectron spectrum are analyzed in terms of the interference of multiple free electron wave packets resulting in multiple partial photoelectron spectra which are coherently added up to yield the observed spectrum. Each wave packet arises from the ionization during different subpulses with different AT splittings, different weights of the AT components, and different quantum mechanical phases due to the time delay T. Partial photoelectron spectra from the subpulses with ($n=0$) and ($n=1$) are shown in Fig. 13(c). The main contribution to the photoelectron spectrum—which is strongly asymmetric—originates from the central subpulse, whereas the adjacent prepulse delivers only a small—more symmetric—contribution. However, due to the coherent superposition of both spectra, the interference structures due to the weak heterodyned signal are very pronounced. Again the fringe spacing $2\pi\hbar/T$ is determined by the temporal separation of the subpulses as indicated in Fig. 13(c). Generally, the detailed physical mechanism of how the modulation amplitude A controls the photoelectron spectrum is intricate but traceable. As shown in Sec. I B the modulation amplitude controls the relative intensities of the subpulses. As far as the strong-field *dynamic* is concerned, for a given optical phase of the pulse sequence, variations of the pulse area of each subpulse introduce changes of the quantum mechanical phase. An increase of the pulse area by π, i.e., half a Rabi cycle, introduces a change of the relative quantum mechanical phase of the amplitudes c_a and c_b by π. Control on the

quantum mechanical phase exerted by the laser intensity was experimentally demonstrated in [19]. Therefore, the modulation amplitude A controls dressed states population via the pulse intensity. As far as the *photoelectron spectrum* is concerned, each subpulse produces a partial photoelectron spectrum, as shown above for one particular choice of A, whose symmetry properties are determined by the dressed state population, and whose energy splitting $\hbar|\Omega|$ is determined by the *absolute* subpulse intensity. These partial photoelectron spectra interfere to produce the measured spectrum where the fringe spacing is given by the temporal separation of the subpulses and the modulation depth of the fringes depends on the *relative* intensities of the subpulses. Control of the AT doublet via the modulation amplitude A demonstrates that transient SPODS is sustained over many subpulses. This example shows that an exact realization of SPODS is not required in order to exert control on the AT doublet. This emphasizes the robustness of the scheme also from the theoretical perspective in accordance with the experimental observations.

V. CONCLUSION

In this contribution we presented a systematic study of strong-field quantum control using sinusoidal phase modulation as a prototype for complex shaped pulses. The influence of all the parameters characterizing this type of phase modulation on the dynamics in the neutral atoms and photoelectron spectra was studied theoretically and experimentally. The dynamics induced by these pulses is particularly interesting because strong-field laser matter interaction with pulses featuring time varying temporal phases can neither be described by perturbative techniques nor using the pulse area as in the case of so-called *real* fields. A natural physical interpretation of the strong-field dynamics was given in terms of the dressed states. Control was achieved by SPODS. In the experiment the free electron wave packets served as convenient target states to map SPODS. The physical mechanism of SPODS by pulse sequences was decomposed into elementary steps. Besides some weak-field interaction with pre-pulses and postpulses SPODS relies on a two-step strong-field process in which the first pulse prepares a state of maximum coherence, whereas the subsequent (most intense) pulse populates a single dressed state. Control is exerted by the relative phase between these pulses. Sinusoidal phase modulation is particularly suitable to realize SPODS because it naturally delivers pulse sequences with adjustable relative intensity and phase. Because virtually all photoelectrons are generated during the most intense pulse, a simple interpretation of the resulting photoelectron spectra could be presented. Unlike the well-known AT spectra, SPODS-photoelectron spectra consist of a single peak at high (low) energies if the upper (lower) dressed state is selectively populated. Numerical studies confirm the applicability of coherent control of molecular dynamics via SPODS on a generic model system [30] and on K_2 dimers [31]. Similar to the experimental findings on atoms these simulations showed that strong-field quantum control by SPODS applied to molecules combines high selectivity (in the order of 80%) and tunability (in the order or 2000 cm^{-1}) with efficient ultrafast population transfer. Just as in atoms, the discontinuities of the optical phase studied in this contribution act as an ultrafast switch among different final states of the molecule. Experiments on larger systems are currently investigated in our labs.

ACKNOWLEDGMENTS

The technical assistance by O. Graefe, the financial support of the Deutsche Forschungsgemeinschaft, and the NRC-Helmholtz program are gratefully acknowledged.

APPENDIX: DRESSED STATE ANALYSIS

In this Appendix we specialize the established theoretical framework of coherent excitation of two-state atoms [22,38,46–51] to the interaction with *shaped* intense laser pulses with regard to SPODS. So far, our experimental results are interpreted in terms of the bare state and the dressed state dynamics. The Bloch picture—connecting both pictures—is discussed in Sec. 1. Because the dynamics of the Bloch vector is particularly suited to study the influence of the temporal phase of the driving field, a detailed analysis of the excitation process with sinusoidally spectrally modulated femtosecond laser pulses in the Bloch picture is given in Sec. 2. This example shows how control is exerted by phase jumps rather than a continually varying temporal phase as discussed in [21]. The coherence properties of the light field and quantum system required for SPODS are discussed in Sec. 3. The observed photoelectron spectra are interpreted in terms of SPODS. Hence, in Sec. 4 we show that in our experiment the photoelectron spectra map the population of the dressed states rather than the bare states.

We start with a summary of the notation used to describe the interaction of shaped pulses with two-state atoms. The temporal (analytic) electric field $E^+(t)=\mathcal{E}^+(t)e^{i\omega_0 t}$ is characterized by its (complex) envelope $\mathcal{E}^+(t)$ and the laser carrier frequency ω_0 [35]. The envelope is written as $\mathcal{E}^+(t)=|\mathcal{E}^+(t)|e^{i\chi(t)}$, where $\chi(t)$ is the temporal phase function. In general, the laser frequency ω_0 is detuned from the transition frequency by $\delta=\omega_{ba}-\omega_0$. The Rabi frequency $\hbar\Omega(t)=\mu\mathcal{E}^+(t)$ is used to define the pulse area $\theta=\int_{-\infty}^{\infty}\Omega(t)dt$. Using the above definitions the bare state Hamiltonian of a two-level atom is written as

$$H=-\frac{\hbar}{2}\begin{pmatrix}\delta & |\Omega|e^{i\chi}\\ |\Omega|e^{-i\chi} & -\delta\end{pmatrix}. \tag{A1}$$

The explicit time dependence of the temporal phase $\chi(t)$ and the Rabi frequency $\Omega(t)$ is suppressed in this shorthand notation. The dressed state picture is obtained from the bare state picture using the unitary transformation

$$T(\Theta,\chi)=\begin{pmatrix}e^{-i\chi/2}\cos(\Theta) & e^{i\chi/2}\sin(\Theta)\\ -e^{-i\chi/2}\sin(\Theta) & e^{i\chi/2}\cos(\Theta)\end{pmatrix}, \tag{A2}$$

with the mixing angle Θ

$$\tan(2\Theta) = \frac{|\Omega|}{\delta}, \tag{A3}$$

i.e., the lower and upper dressed state amplitudes $d_l(t)$ and $d_u(t)$ are connected to the bare state amplitudes $c_a(t)$ and $c_b(t)$ by

$$\begin{pmatrix} d_l(t) \\ d_u(t) \end{pmatrix} = T(\Theta,\chi)\begin{pmatrix} c_a(t) \\ c_b(t) \end{pmatrix}. \tag{A4}$$

1. Bloch vector indicates the dressed state population

First, we recall that SPODS is equivalent to a stationary Bloch vector $\rho(t)$ during the laser interaction which implies that the angular velocity vector Ω_B is (anti-) parallel to the Bloch vector throughout the laser pulse. To this end, we consider the system in a single dressed state $[|d_u(t)|^2=1]$. For instance, in the dressed state basis, the time evolution in the upper dressed state reads

$$\begin{pmatrix} d_l(t) \\ d_u(t) \end{pmatrix} = \begin{pmatrix} 0 \\ e^{-i\omega_u t} \end{pmatrix}, \tag{A5}$$

where $\hbar\omega_u$ describes the upper dressed state energy. The transformation to the bare state basis is obtained by multiplication with $T^{\dagger}(\Theta,\chi)$

$$\begin{pmatrix} c_a(t) \\ c_b(t) \end{pmatrix} = T^{\dagger}(\Theta,\chi)\begin{pmatrix} d_l(t) \\ d_u(t) \end{pmatrix}. \tag{A6}$$

The bare state amplitudes $c_a(t)$ and $c_b(t)$ obtained from Eq. (A6) are used to yield the Bloch vector

$$\rho(t) = \begin{pmatrix} c_a^* c_b + c_a c_b^* \\ i(c_a^* c_b - c_a c_b^*) \\ |c_b|^2 - |c_a|^2 \end{pmatrix} = \begin{pmatrix} -\cos(\chi)\sin(2\Theta) \\ -\sin(\chi)\sin(2\Theta) \\ \cos(2\Theta) \end{pmatrix}, \tag{A7}$$

which is time independent ($\dot{\rho}=0$) throughout the interaction with the laser field if the optical phase χ and the mixing angle Θ are constant. With the equation of motion for the Bloch vector $\dot{\rho}(t)=\Omega_B(t)\times\rho(t)$ it follows that the angular velocity vector Ω_B is (anti-) parallel to the Bloch vector ρ since $\Omega_B \| \rho$ implies $\dot{\rho}=0$. Upon comparison of the angular velocity vector

$$\Omega_B = \begin{pmatrix} -|\Omega|\cos(\chi) \\ -|\Omega|\sin(\chi) \\ \delta \end{pmatrix} \tag{A8}$$

with the Bloch vector of Eq. (A7) and using the definition of the mixing angle of Eq. (A3) we find that the vectors $\rho(t)$ and Ω_B are parallel if the upper dressed state is selectively populated. Accordingly, the lower dressed state is selectively populated if $\rho(t)$ and Ω_B are antiparallel. The condition for SPODS, i.e., $\Omega_B \| \pm\rho$ shows that SPODS can be realized with off-resonance pulsed excitation as well. We can use Eq. (A8) to design shaped off-resonant SPODS pulses considering that δ needs to be proportional to $|\Omega|$ throughout the whole excitation process which implies largest detuning at the peak intensity. Generally, pulsed SPODS requires a constant value of the mixing angle during the pulse which is always true for resonant excitation because the mixing angle is $\pi/4$ irrespective of the laser intensity. As a consequence, resonant selective population of a single dressed state can be maintained with shaped laser pulses of any (time varying) intensity as long as the optical phase remains constant (or jumps by π). As an example, shaped pulses generated by TOD realize $\Omega_B \| \pm\rho$ throughout the complete pulse once $\Omega_B$and ρ have been aligned prior to the TOD pulse.

2. Excitation with sinusoidally phase modulated pulses in the Bloch picture

In this section, we use the Bloch sphere picture in order to analyze the two-level dynamic induced by shaped intense pulses. Since pulses generated by the sinusoidal phase modulation can be decomposed into a sequence of subpulses—provided an appropriate choice of the modulation parameters—the dynamics induced by the nth subpulse will be discussed in terms of the angular velocity vector Ω_n proportional to the peak electrical field of the nth subpulse and its (constant, cf., for instance, Fig. 10) optical phase χ_n. The Bloch sphere representation allows us to consider the bare state dynamics via the inversion $w=|c_b|^2-|c_a|^2$ component of the Bloch vector and the atomic coherence through the position of ρ in the u-v plane, and, simultaneously, to envisage the dressed state dynamics via the relative orientation of the angular velocity vector Ω_n with respect to the Bloch vector ρ. To this end, the trace of the Bloch vector $\rho(t)$ and the angular velocity vectors Ω_0 and $\Omega_{\pm1}$ for the central subpulse ($n=0$) and the adjacent subpulses ($n=\pm1$) are indicated in Fig. 14. The dynamics of the Bloch vector is determined by the equation of motion $\dot{\rho}(t)=\Omega_B(t)\times\rho(t)$, and hence, the angular velocity vector Ω_B defined in Eq. (A8) controls the motion of $\rho(t)$. The orientation of the angular velocity vector—which is always confined to the u-v plane for resonant excitation—is determined by the optical phase $\chi(t)$ as indicated in Fig. 14(a).

We start with the analysis of the reference case shown in Fig. 14(b) for sinusoidally modulated resonant femtosecond laser pulses using the modulation parameters $A=0.3$, $T=100$ fs, $\phi=\pi/2$ rad, and $\Delta\omega=\pi/50$ fs^{-1}. In Sec. IV, this case was analyzed using both the bare state picture [cf. Fig. 10(b)] and the dressed state picture [cf. Fig. 10(d)]. The first subpulse ($n=2$) leads to a weak-field excitation. Since the ground state is not significantly depleted, i.e., $|c_a|^2\approx1$, implying $w\approx-1$, the Bloch vector stays at the south pole. During the second subpulse ($n=1$), the angular velocity vector Ω_1 is aligned along the $-v$ direction due to the optical phase of $\chi_1=\pi/2$. The phase jump leads to the sharp bend of the Bloch vector trace in the vicinity of the south pole. Since this subpulse has a pulse area of $\pi/2$, the Bloch vector comes to a rest close to the $+u$ direction. During the central subpulse ($n=0$), the angular velocity vector Ω_0 points in the $-u$ direction due to the optical phase of $\chi_0=0$, i.e. (approximately) *antiparallel* to the Bloch vector. In this configuration, the equation of motion for the Bloch vector reads $\dot{\rho}(t)=\Omega_B\times\rho \approx 0$, which implies that $\rho(t)$ is (approximately) stationary

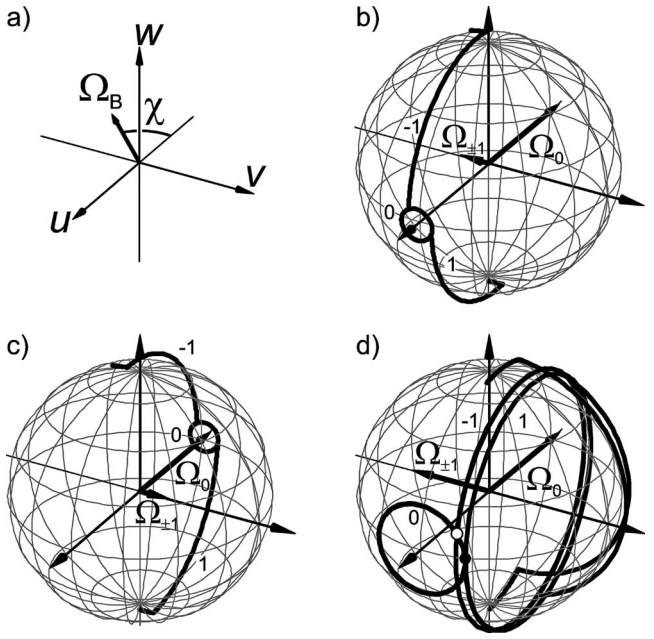

FIG. 14. Bloch sphere representation $\rho(t)$ of the dynamics induced by the excitation of ground state atoms $\rho(-\infty)=\{0,0,-1\}$ with sinusoidally modulated resonant femtosecond laser pulses in the frame rotating with the central laser frequency. The modulation parameters are $A=0.3$, $T=100$ fs, $\phi=\pi/2$ rad, and $\Delta\omega=\pi/50$ fs^{-1}. (a) shows how the optical phase χ controls the position of the angular velocity vector Ω_B defined in Eq. (A8). The Bloch representation of the reference case as depicted in Fig. 10 is shown in (b). The dynamics upon variation of the time ($T=150$ fs, cf. Fig. 11) shown in (c) is identical with the dynamics upon variation of the phase ($\phi=-\pi/2$, cf. Fig. 12). The dynamics for an amplitude of $A=1$ and a field of $2.3\times\mathcal{E}_{in}^{+}$ (cf. Fig. 13) is shown in (d). The angular velocity vectors Ω_0 and $\Omega_{\pm1}$ proportional to the peak electrical fields of the most intense subpulse ($n=0$) and the adjacent prepulses ($n=\pm1$) are indicated in order to emphasize the orientation of $\Omega_B(t)$ and $\rho(t)$ which determines the transient SPODS. In panel (d) the black dot indicates the transition from the prepulse ($n=1$) to the central subpulse, whereas the white dot marks the transition to the first postpulse ($n=-1$).

during this subpulse. Note that the initial conditions prepared by the $n=1$ subpulse have been set slightly besides the exact realization of $\Omega_B\times\rho=0$ in order to emphasize the rotation about the u axis during the central subpulse. As a consequence of ρ being stationary, the population is constant during this subpulse. As shown in the previous section, stationarity of the population is independent of the subpulse intensity and operative for any pulse shape, provided the pulse is *real*. As recapitulated in Sec. 1, if the angular velocity vector is (anti-) parallel to the Bloch vector, a single dressed state is selectively populated. In this case, since $\rho(t)$ and Ω_0 are *antiparallel*, the lower dressed state is selectively populated during the central pulse accounting for the photoelectron spectrum depicted in Fig. 10(c). During the fourth subpulse ($n=-1$) with a phase of $\pi/2$ and a pulse area of $\pi/2$, the angular velocity vector Ω_{-1} is again aligned to the $-v$ axis and therefore the Bloch vector continues its way to the north pole where some weak-field interaction takes place during the last subpulse. Again the phase jump of $\pi/2$ manifests itself as a sharp bend of the Bloch vector trace.

Figure 14(c) shows the dynamics of the Bloch vector for a phase function with $T=150$ fs leaving the other parameters unchanged. This case was discussed in the context of Fig. 11 in Sec. IV. The value of $T=150$ fs delivers the absolute phase of $-n\pi/2$ for each subpulse leading to phase jumps of $\pi/2$ between adjacent prepulses [cf. Fig. 11(a)]. Due to the absolute phase of $\chi_2=-\pi$ of the first weak pulse ($n=2$), the angular velocity vector Ω_2 (not displayed) points in the $+u$ direction. However, in contrast to (b), the phase of the second subpulse ($n=1$) is $-\pi/2$ and, therefore, Ω_1 is oriented in the $+v$ direction. As a consequence, at the end of the second $\pi/2$ subpulse the Bloch vector is (approximately) *parallel* to the $-u$ direction. Because the absolute phase of the central subpulse is zero for all pulse sequences considered here, the Bloch vector and the angular velocity vector Ω_0 are *parallel* during the central pulse. This configuration is the alternative implementation of $\Omega_B\times\rho\approx0$, which implies an (approximately) constant population during the central subpulse. This configuration corresponds to the selective population of the upper dressed state. Hence, the dynamics in the Bloch picture readily accounts for the shape of photoelectron spectrum. Comparison of Figs. 14(b) and 14(c) clearly reveals the physical mechanism of SPODS. Control on *which* dressed state is selectively populated is exerted by the $\pi/2$ subpulse ($n=1$) that orients the vectors ρ and Ω_0 either *parallel* or *antiparallel* during the central subpulse. This is equivalent to the above statement that the relative phase between the prepulse ($n=1$) and the central pulse ($n=0$) determines the dressed state population provided a state of maximum coherence was prepared by the ($n=1$) prepulse. Another way to produce phase jumps of $\pi/2$ between adjacent prepulses is realized by the absolute phase of the modulation function set to $\phi=-\pi/2$ as shown in Fig. 12(a). Although the temporal separation between the subpulses is reduced to $T=100$ fs, i.e., the phase mask and pulse shape are different in comparison to that of Fig. 11(a), the Bloch vector trace is identical with the one shown in Fig. 14(c). Since the time enters only parametrically in the Bloch vector trace, these details of the pulse shape are not seen. Therefore, the Bloch picture is well suited to extract the essence of the physical mechanism for SPODS. Note however, that the photoelectron spectra shown in Figs. 11(c) and 12(c) are not identical due to the different delays of the interfering free electron wave packets.

The last case, presented in Fig. 14(d), is devoted to the analysis of the Bloch vector dynamics induced by a pulse generated with a larger modulation amplitude ($A=1$) and an increased electrical field. Obviously, the dynamic of the Bloch vector is more complex and thus represents a less idealized case compared to Figs. 14(b) and 14(c). This allows us to elucidate important general relations between the Bloch representation, the dressed state population, and the photoelectron spectra. As seen in Fig. 13(a) the pulse sequence consists of seven subpulses with the absolute phases of $n\pi/2$. The first subpulse ($n=3$) with an optical phase of $\chi_3=-\pi/2$ (and hence the angular velocity vector Ω_3 parallel to $+v$) leads to a weak-field interaction with the atom, as seen before. The next subpulse ($n=2$) with a pulse area larger than $\pi/2$ transfers the Bloch vector into the northern

hemisphere. Due to its optical phase of $\chi_2=\pi$, the angular velocity vector Ω_2 (not shown) is *parallel* to $+u$. Because the Bloch vector has a nonvanishing component *antiparallel* to Ω_2 during this subpulse, the lower dressed state is preferentially populated [cf. Fig. 13(d)]. A similar configuration is found during the third subpulse ($n=1$), where the Bloch vector rotates about the angular velocity vector Ω_1 parallel to the $-v$ axis. The high Rabi frequency gives rise to several Rabi nutations about the v axis. Here, the Bloch vector has always a nonvanishing component along the $+v$ direction. As shown in Fig. 13(d), the lower dressed state is preferentially—though not completely selectively—populated. After this pulse, the Bloch vector stops approximately aligned to the $+u$ axis as indicated with the black dot in Fig. 14(d). During the central subpulse ($n=0$) with the optical phase of $\chi_0=0$ the Bloch vector rotates almost three times about the u axis. Since ρ and Ω_0 are approximately *antiparallel* during this subpulse, the lower dressed state is populated with high selectivity as depicted in Fig. 13(d). The Bloch vector for the first postpulse ($n=-1$) starts at the position indicated with the white dot in Fig. 14(d). Since the optical phase of $\chi_{-1}=\pi/2$ and the angular velocity vector Ω_{-1} agree with those of the first prepulse ($n=1$), and, in addition, the initial condition is located close to the orbit of $\rho(t)$ during the ($n=1$) prepulse, the same motion of $\rho(t)$ takes place during the first postpulse. This leads again to preferential population of the lower dressed state, but in this case, with slightly lower selectivity as compared to the ($n=1$) prepulse, because the orbit is closer to the w axis as seen in Fig. 14(d). The second postpulse ($n=-2$) induces a similar dynamic as the second prepulse, because the optical phases $\chi_{\pm 2}=\pi$, and hence the angular velocity vectors $\Omega_{\pm 2}$ are identical. Again the lower dressed state is slightly more populated than the upper dressed state. These examples show that the inspection of the Bloch vector and the angular velocity vector allows us to extract the control mechanism and to qualitatively predict the photoelectron spectrum being the image of the control mechanism.

3. Phase condition for SPODS

In this section the coherence properties of the shaped pulses and the excited atom to create SPODS are investigated. To this end, we consider for simplicity resonant two-pulse excitation from the ground state, i.e., the mixing angle Θ is always $\pi/4$. The action of the first pulse with an optical phase of χ_1 and a pulse area of θ_1 exciting ground state atoms is described by the resonant time evolution operator $U_\infty(\theta_1,\chi_1)$ [49]

$$U_\infty(\theta_1,\chi_1)=\begin{pmatrix}\cos(\theta_1/2) & i\,e^{i\chi_1}\sin(\theta_1/2)\\ i\,e^{-i\chi_1}\sin(\theta_1/2) & \cos(\theta_1/2)\end{pmatrix}\begin{pmatrix}1\\0\end{pmatrix}. \tag{A9}$$

For resonant excitation with a first $\theta_1=\pi/2$ pulse and a second pulse with the constant optical phase χ_2, the initial dressed state amplitudes are found to be

$$\begin{pmatrix}d_l\\ d_u\end{pmatrix}=T(\pi/4,\chi_2)U_\infty(\pi/2,\chi_1)\begin{pmatrix}1\\0\end{pmatrix}. \tag{A10}$$

Because the dressed states are the eigenstates of the light matter interaction, the dressed state population—given by the squared absolute values of the dressed state amplitudes—remains constant during the interaction with the second pulse. Evaluation of Eq. (A10) yields the dressed states population

$$|d_l|^2=\tfrac{1}{2}[1-\sin(\Delta\chi)] \tag{A11}$$

$$|d_u|^2=\tfrac{1}{2}[1+\sin(\Delta\chi)] \tag{A12}$$

as a function of the optical phases of the pulse sequence where $\Delta\chi=\chi_2-\chi_1$ describes the difference of the optical phases of the first and the second subpulse. As a consequence a phase jump of $\Delta\chi=\pi/2$ leads to $|d_u(t)|^2=1$, i.e., selective population of the upper dressed state whereas a relative phase of $\Delta\chi=-\pi/2$ exclusively populates the lower dressed state.

4. Photoelectron spectra map dressed state population

In order to see that the photoelectron spectrum maps the dressed states population, we consider an idealized scenario in which the atom is in the lower dressed state with a constant probability of $\cos^2(\vartheta)$ and in the upper dressed state with a constant probability of $\sin^2(\vartheta)$. This is realized by the amplitudes

$$\begin{pmatrix}d_l(t)\\ d_u(t)\end{pmatrix}=\begin{pmatrix}\cos(\vartheta)e^{-i\omega_l t}\\ \sin(\vartheta)e^{-i\omega_u t}\end{pmatrix} \tag{A13}$$

in the dressed state basis. For clarity we assume resonant excitation and an optical phase of $\chi=0$ to obtain the excited bare state amplitude using Eq. (A6)

$$c_b(t)=\frac{1}{\sqrt{2}}[\cos(\vartheta)e^{-i\omega_l t}+\sin(\vartheta)e^{-i\omega_u t}]. \tag{A14}$$

Since the photoelectron amplitudes are described by the Fourier transform of the excited state amplitude windowed by some power of electrical field $\mathcal{F}(t)=[\mathcal{E}^-(t)]^n$ [cf. Eq. (1)] the amplitudes for the photoelectrons read

$$c(\omega_e)\propto\cos(\vartheta)\tilde{\mathcal{F}}(\omega+|\Omega|/2)+\sin(\vartheta)\tilde{\mathcal{F}}(\omega-|\Omega|/2), \tag{A15}$$

where $\tilde{\mathcal{F}}(\omega)$ is the Fourier transform of $\mathcal{F}(t)$ and we make use of the Fourier shift theorem and insert the resonant dressed state energies $\omega_l=-\frac{1}{2}|\Omega|$ and $\omega_u=\frac{1}{2}|\Omega|$. Equation (A15) shows that the weights of the AT components are $\cos^2(\vartheta)$ and $\sin^2(\vartheta)$ for the lower and upper dressed states, respectively. In this simplified picture the photoelectron spectrum *exactly* maps the population of the dressed states. Obviously, this description somehow oversimplifies the ionization process since the dressed state population $\vartheta(t)$ and the dressed state energy splitting $\hbar\Omega(t)$ are controlled by the

laser field and therefore both quantities are generally time dependent. However, since most photoelectrons are produced at the highest laser intensity, i.e., for approximately constant values of ϑ and $\hbar\Omega$, the approximation is justified during the time interval of ionization with highest probability. From a physical point of view, it is comprehensible that in this simultaneous excitation and ionization scheme—where photoelectrons are generated during the strong-field laser-atom interaction—the dressed states rather than the bare states are mapped into the photoelectron spectrum.

[1] S. A. Rice and M. Zhao, *Optical Control of Molecular Dynamics* (Wiley-Interscience, New York, 2000).

[2] M. Shapiro and P. Brumer, *Principles of the Quantum Control of Molecular Processes* (John Wiley & Sons, Hoboken, 2003).

[3] M. Wollenhaupt, V. Engel, and T. Baumert, Annu. Rev. Phys. Chem. **56**, 25 (2005).

[4] T. Brixner, T. Pfeifer, G. Gerber, M. Wollenhaupt, and T. Baumert, in *Femtosecond Laser Spectroscopy*, edited by P. Hannaford (Springer, New York, 2005), Chap. 9.

[5] M. Dantus and V. V. Lozovoy, Chem. Rev. (Washington, D.C.) **104**, 1813 (2004).

[6] R. S. Judson and H. Rabitz, Phys. Rev. Lett. **68**, 1500 (1992).

[7] A. M. Weiner, Rev. Sci. Instrum. **71**, 1929 (2000).

[8] T. Baumert, T. Brixner, V. Seyfried, M. Strehle, and G. Gerber, Appl. Phys. B **65**, 779 (1997).

[9] D. Yelin, D. Meshulach, and Y. Silberberg, Opt. Lett. **22**, 1793 (1997).

[10] C. J. Bardeen, V. V. Yakolev, K. R. Wilson, S. D. Carpenter, P. M. Weber, and W. S. Warren, Chem. Phys. Lett. **280**, 151 (1997).

[11] A. Assion, T. Baumert, M. Bergt, T. Brixner, B. Kiefer, V. Seyfried, M. Strehle, and G. Gerber, Science **282**, 919 (1998).

[12] R. Bartels, S. Backus, I. Christov, H. Kapteyn, and M. Murnane, Chem. Phys. Lett. **267**, 277 (2001).

[13] T. Feurer, A. Glaß, T. Rozgonyi, R. Sauerbrey, and G. Szabo, Chem. Phys. Lett. **267**, 223 (2001).

[14] J. L. Herek, W. Wohlleben, R. J. Cogdell, D. Zeidler, and M. Motzkus, Nature (London) **417**, 533 (2002).

[15] R. J. Levis and H. A. Rabitz, J. Phys. Chem. **106**, 6427 (2002).

[16] T. Brixner and G. Gerber, ChemPhysChem **4**, 418 (2003).

[17] C. Daniel, J. Full, L. Gonzales, C. Lupulescu, J. Manz, A. Merli, S. Vajda, and L. Wöste, Science **299**, 536 (2003).

[18] M. Wollenhaupt, A. Präkelt, C. Sarpe-Tudoran, D. Liese, and T. Baumert, J. Opt. B: Quantum Semiclassical Opt. **7**, S270 (2005).

[19] M. Wollenhaupt, A. Assion, O. Bazhan, Ch. Horn, D. Liese, C. Sarpe-Tudoran, M. Winter, and T. Baumert, Phys. Rev. A **68**, 015401 (2003).

[20] N. Dudovich, T. Polack, Avi Pe'er, and Y. Silberberg, Phys. Rev. Lett. **94**, 083002 (2005).

[21] M. Wollenhaupt, A. Präkelt, C. Sarpe-Tudoran, D. Liese, and T. Baumert, Appl. Phys. B **82**, 183 (2006).

[22] Pierre Meystre and Murray Sargent, III. *Elements of Quantum Optics*, 3rd ed. (Springer-Verlag, Berlin, 1990).

[23] S. A. Hosseini and D. Goswami, Phys. Rev. A **64**, 033410 (2001).

[24] A. M. Weiner, D. E. Leaird, G. P. Wiederrecht, and K. A. Nelson, Science **247**, 1317 (1990).

[25] N. Dudovich, B. Dayan, S. M. Gallagher Faeder, and Y. Silberberg, Phys. Rev. Lett. **86**, 47 (2001).

[26] V. V. Lozovoy, I. Pastirk, A. Walowicz, and M. Dantus, J. Chem. Phys. **118**, 3187 (2003).

[27] A. Bartelt, A. Lindinger, C. Lupulescu, Š. Vajda, and L. Wöste, Phys. Chem. Chem. Phys. **5**, 3610 (2004).

[28] A. Präkelt, M. Wollenhaupt, C. Sarpe-Tudoran, and T. Baumert, Phys. Rev. A **70**, 063407 (2004).

[29] M. Wollenhaupt, A. Präkelt, C. Sarpe-Tudoran, D. Liese, and T. Baumert, J. Mod. Opt. **52**, 2187 (2005).

[30] M. Wollenhaupt, D. Liese, A. Präkelt, C. Sarpe-Tudoran, and T. Baumert, Chem. Phys. Lett. **419**, 184 (2006).

[31] M. Wollenhaupt and T. Baumert, J. Photochem. Photobiol., A, **180**, 248 (2006).

[32] H. B. Bebb and A. Gold, Phys. Rev. **143**, 1 (1966).

[33] Ch. Meier and V. Engel, Phys. Rev. Lett. **73**, 3207 (1994).

[34] D. Meshulach and Y. Silberberg, Phys. Rev. A **60**, 1287 (1999).

[35] J. C. Diels and W. Rudolph, *Ultrashort Laser Pulse Phenomena* (Academic Press, San Diego, 1996).

[36] S. H. Autler and C. H. Townes, Phys. Rev. **100**, 703 (1955).

[37] Eric W. Weisstein, *Jacobi-Anger Expansion. From MathWorld — A Wolfram Web Resource*. Available at http://mathworld.wolfram.com/Jacobi-AngerExpansion.html.

[38] Bruce W. Shore, *The Theory of Coherent Atomic Excitation, Volume 1: Simple Atoms and Fields* (John Wiley, New York, 1990).

[39] A. Präkelt, M. Wollenhaupt, A. Assion, Ch. Horn, C. Sarpe-Tudoran, M. Winter, and T. Baumert, Rev. Sci. Instrum. **74**, 4950 (2003).

[40] M. Wollenhaupt, A. Assion, D. Liese, C. Sarpe-Tudoran, T. Baumert, S. Zamith, M. A. Bouchene, B. Girard, A. Flettner, U. Weichmann, and G. Gerber, Phys. Rev. Lett. **89**, 173001 (2002).

[41] L. Lepetit, G. Chériaux, and M. Joffre, J. Opt. Soc. Am. B **12**, 2467 (1995).

[42] P. O'Shea, M. Kimmel, X. Gu, and R. Trebino, Opt. Lett. **26**, 932 (2001).

[43] S. R. Hartmann and E. L. Hahn, Phys. Rev. **128**, 2042 (1962).

[44] Y. S. Bai, A. G. Yodh, and T. W. Mossberg, Phys. Rev. Lett. **55**, 1277 (1985).

[45] E. T. Sleva, I. M. Xavier, and A. H. Zewail, J. Opt. Soc. Am. B **3**, 483 (1986).

[46] R. P. Feynman, F. L. Vernon, and R. W. Hellwarth, J. Appl. Phys. **28**, 49 (1957).

[47] L. Allen and J. H. Eberly, *Optical Resonance and Two-Level Atoms* (Dover Publications, New York, 1987).

[48] Claude Cohen-Tannoudji, Jacques Dupont-Roc, and Gilbert Grynberg, *Atom-Photon Interactions, Basic Processes and Applications* (John Wiley, New York, 1992).

[49] Shaul Mukamel, *Principles of Nonlinear Optical Spectroscopy* (Oxford University Press, New York, 1995).

[50] N. V. Vitanov, M. Fleischhauer, B. W. Shore, and K. Bergmann, Adv. At., Mol., Opt. Phys. **46**, 55 (2001).

[51] D. Goswami, Phys. Rep. **374**, 385 (2003).